Korean J. Chem. Eng., 40(4), 791-801 (2023)
DOI: 10.1007/s11814-022-1317-7

pISSN: 0256-1115
eISSN: 1975-7220

Enhanced desulfurization performance of copper aerogel-based absorbents

Jungwon Yun*,, Dohyung Kang***, Ramya Ramkumar*, Dongjoon Kim**, Seung Jong Lee****, Yongseung Yun****, Woo Kyoung Kim*,†, No-Kuk Park*****,†, and Minkyu Kim*,†**

*School of Chemical Engineering, Yeungnam University, 280 Daehak-ro, Gyeongsan, Gyeongbuk 38541, Korea
**William G. Lowrie Chemical and Biomolecular Engineering, The Ohio State University, Columbus, Ohio 43210, USA
***Department of Future Energy Convergence, Seoul National University of Science & Technology, 232 Gongreung-ro, Nowon-gu, Seoul 01811, Korea
****Institute for Advanced Engineering, 175-28, Goan-ro 51 beon-gil, Baegam-myeon, Cheoin-gu, Yongin-si, Gyeonggi-do 17180, Korea
*****Institute of Clean Technology, Yeungnam University, 280 Daehak-ro, Gyeongsan, Gyeongbuk 38541, Korea
(*Received 27 July 2022 • Revised 19 September 2022 • Accepted 12 October 2022*)

Abstract−Copper aerogel was employed as a sulfur absorbent to enhance desulfurization performance. The copper aerogel was synthesized using an ethanolic approach and dried by three different drying techniques of freeze drying, organic solvent sublimation drying with tert-butanol, and acetonitrile. The typical interconnecting and porous structure of the aerogel was clearly observed only for the aerogel sample made by freeze-drying. Further desulfurization tests showed that freeze-dried copper aerogel had the highest sulfur capacity (12 mgS/g-sorbent) at a low temperature of 200 °C. This enhancement was driven by two factors. 1) The interconnecting structure of copper aerogel weakens the gas diffusion resistance, which can prevent the gas from flowing the inside of sample thereby reducing the efficiency of absorbent. 2) The partially oxidized structure of Cu_2O is thermodynamically active toward the desulfurization reaction, which was confirmed by density functional theory calculations. Overall, using copper aerogels with an interconnecting structure and Cu_2O composition would be a novel approach to enhance desulfurization performance.

Keywords: Desulfurization, Copper Aerogel, Gas Diffusion Resistance, Cu_2O (111)

INTRODUCTION

Hydrogen energy has attracted considerable attention as an alternative to fossil fuels [1] because of its environmentally friendly features, producing only water as the by-product of an oxidation-controlled reaction [2]. The magnitude of eco-friendliness for hydrogen energy is strongly dependent on the way of hydrogen production, including green, blue, and grey hydrogen [3]. The production of green hydrogen does not involve the generation of greenhouse gases, such as CO_2(g); water splitting ($H_2O \rightarrow H_2+½O_2$) and methane pyrolysis ($CH_4 \rightarrow C+2H_2$(g)) are the examples of green hydrogen production [4]. Because of its non-CO_2 production, green hydrogen is the ultimate goal to resolve current and future environmental issues; however, reducing the production cost is non-trivial because of the current low-level technologies [5]. Blue hydrogen can act as a bridge in the energy transition from fossil fuels to hydrogen because of its low production cost with CO_2 capture-storage [6]. Therefore, blue hydrogen utilizing fossil fuels, such as petroleum coke and natural gas, to produce hydrogen take a large market share in hydrogen production [7-9]. Within blue hydrogen production, the gasification of petroleum coke is promising for generating hydrogen [10-12]. The gasification produces syngas [10], including sulfur compounds, which potentially deactivates and lowers the durability of the fuel cell catalysts for hydrogen production [13]. As a result, a desulfurization process of removing sulfur compounds is a critical step to producing high purity hydrogen [14].

There are diverse desulfurization processes, including hydrodesulfurization, extraction, oxidation, and adsorption [15-17]. Recently, metal oxides, such as ZnO, Fe_2O_3, MnO_2, and CuO, have been studied extensively as sulfur absorbents because metal oxides provide high reactivity and sulfur capacity [18-22]. In particular, copper-based sorbents have been proposed to be highly active toward desulfurization at low temperatures (<400 °C) [14,23-25]. Cuprous species can form a π-complex with sulfur compound at ambient conditions, which leads to high activity as absorbents [26]. Zhang et al. reported the excellent desulfurization performance of a Cu_2O-SiO_2 nanocomposite [27], and similar high performance has been achieved from other Cu_2O nanoparticles [28]. This is because Cu_2O has enhanced π-complexation between Cu(I) and sulfur compounds [27], indicating more active sites of absorbents, resulting in the high desulfurization performance.

Nevertheless, typical absorbents have a critical challenge: gas diffusion resistance (GDR) [29-33]. GDR prevents activation of the remaining active sites in the desulfurization process, which leads to low performance. Many studies to weaken the GDR of absorbents have been conducted [34-38]. Wang et al. weakened the resistance for CO_2 absorbents of SBA-15 using an amine dendrimer. They applied melamine-based and acrylate-based amine dendrimers to SBA-15, and those amine compounds created spaces between den-

†To whom correspondence should be addressed.
E-mail: wkim@ynu.ac.kr, nokukpark@ynu.ac.kr, mk_kim@ynu.ac.kr

dritic branches, thereby enhancing GDR [39]. In addition, Kiwi-Minsker et al. deposited nanoparticles (NPs), such as La_2O_3, CaO, MgO, ZnO, and Al_2O_3 on activated carbon fibers (ACF). The results showed that the capacity of the absorbents for acetaldehyde is increased because the presence of macrostructure weakens GDR [40]. In particular, for the sulfur absorbent, Park et al. developed CuO absorbents supported by macroporous alumina. The macro pores of support trigger a decrease in GDR, resulting in ~1.4 times higher sulfur capacity than the CuO absorbents on non-macroporous alumina [14]. Another novel approach to weaken GDR can be the application of aerogels to the desulfurization reaction. Specifically, aerogels are lightweight with low density, large volume, high surface area, and high porosity [41-44]. The remarkably porous structure of aerogels potentially weakens the gas diffusion resistance [45-47].

In this study, a copper aerogel was applied to the desulfurization reaction because it has two benefits for the desulfurization kinetics: 1) oxide phases having high reactivity toward desulfurization, and 2) the porous structures improving the gas diffusion resistance. Three differently made copper aerogels were synthesized, characterized, and compared. The optimized ethanolic approach was used to synthesize a copper hydrogel, and dried by freeze-drying (FD) and organic solvent (tert-butanol (TB) and acetonitrile (ACN)) sublimation drying (OSSD) [48-50]. The further characterization confirmed that the samples made by FD and OSSD (TB) show the typical aerogel features of network-like structures while OSSD (ACN) does not, but it is oxidized to CuO. Owing to the absence of aerogel features of OSSD (ACN), this study focused only on the samples of FD and OSSD (TB) for desulfurization tests. The desulfurization results showed that FD provides higher sulfur capacity than OSSD (TB). Combined with the characterization results, it was confirmed that the weakened gas diffusion resistance by the network-like structure, which is formed more clearly in the FD aerogel, is attributed to the higher sulfur capacity. Density functional theory (DFT) calculations were also conducted to understand the COS desulfurization kinetics of the Cu_2O phase observed in FD and OSSD (TB) aerogels. The simulation predicted that the desulfurization reaction is thermodynamically favorable on the Cu_2O phase, and the COS desulfurization reaction is even more favorable on the Cu_2O phase compared to CuO phase [14]. Overall, this novel approach using the network-like structure of aerogels and the active phase of Cu_2O provides significant improvement in desulfurization reaction. Based on these results, we conclude that copper aerogel would be a good candidate for desulfurization absorbent.

1. Preparation of Cu Aerogel

An ethanolic approach was used to prepare the Cu aerogel, which reduces copper ions to metallic copper using a reducing agent in an ethanol solvent [50]. The Cu precursor, copper(II) chloride ($CuCl_2$, 99%, Aldrich), was dissolved in an ethanol solution (25 vol% in DI water). The solution was bubbled with flowing N_2 for 20 min. A reducing agent, sodium borohydride ($NaBH_4$, ≥98%, Aldrich), was then added to the solution to achieve a molar ratio of 1 : 10 ($CuCl_2$: $NaBH_4$). $NaBH_4$ reduced $CuCl_2$ resulting in a copper hydrogel by the net reaction of $Cu^{2+} \rightarrow Cu$. After the gel was allowed to settle and age for 30 min, it was washed several times with DI water and ethanol to remove the remaining salts. These steps were conducted at room temperature. The resulting gel was dried further to form an aerogel through various methods [50].

Among several drying methods, organic solvent sublimation drying and freeze drying were conducted instead of CO_2-utilized supercritical drying, which is used widely. CO_2-utilized supercritical drying has advantages, such as non-flammability, non-toxicity, and sustainability [51], but high-pressure CO_2 can cause safety and cost issues [52]. One possible alternative is organic solvent sublimation drying, which requires less operation time and cost, and avoids the destruction of the pore structure by the surface tension of solvents [52]. Tert-butanol (TB, freezing point: 25.5 °C) and acetonitrile (ACN, freezing point: −45 °C) are possible candidates for OSSD because of their low surface tension and high freezing points [48]. In addition to OSSD methods, the freeze-drying method is also used widely because of its lower cost and lower linear shrinkage than other drying methods [49]. Both the OSSD and FD methods utilize sublimation, so solidification and sublimation are essential steps. The OSSD method involves the dispersion of the copper hydrogel in organic solvents, TB or ACN. The sample was kept in a freezer for 4-6 h and dried in an oven at 50 °C for 24 h to allow evaporation [52]. By contrast, the FD method consisted of the immersion of the copper hydrogels in DI water, and the sample was frozen in a deep freezer at −80 °C for 2 h. Subsequently, the sample was transferred to the freeze dryer at −80 °C and 5 mTorr, and dried for 24-48 h, depending on the solvent volume. Finally, there are three synthesized samples varied with methods: synthesized by OSSD method with 1) tert butanol (OSSD (TB)), 2) OSSD method with acetonitrile (OSSD (ACN)), and 3) FD method with DI water (FD). Since the three different methods would provide different properties of synthesized Cu aerogels, different desulfurization performances would be expected.

2. Characterization

X-ray diffraction (XRD, MPD diffractometer, nickel-filtered CuKα radiation, 40.0 kV and 15.0 mA, Miniflex, Rigaku, Japan) of powder samples was performed from 10° to 80° with a scanning rate of 6 deg/min to confirm their crystal structure. Scanning electron microscopy (SEM, S-4800, HITACHI) images of aerogel particles were recorded with an operating voltage of 10 kV. The textural properties of the particles were measured using N_2 physisorption (3-Flex, Micromeritics) and studied using the Brunauer-Emmett-Teller (BET) and Barrett-Joyner-Halenda (BJH) methods. Before the measurements, the samples were degassed at 180 °C under vacuum overnight. X-ray photoelectron spectroscopy (XPS, K-Alpha X-ray photoelectron spectrometer, Thermo Fisher Scientific, UK) was performed to acquire the chemical states of the aerogel surface.

3. Desulfurization Test

A desulfurization test was performed in a fixed bed reactor system equipped with gas chromatography (GC, Shimadzu GC-8A). The copper aerogel powders (0.2 g) were packed in the 0.5-inch quartz reactor. The sample was heated to 200 °C under N_2 flow. The reaction temperature was monitored using a thermocouple vertically installed inside the reactor. When the temperature reached 200 °C, the N_2 flow was switched to the COS flow (3,000 ppmv diluted by N_2) so that the 130 mL min^{-1} of mixture gas (COS and N_2) was supplied to Cu aerogels. During the desulfurization reaction, the output was monitored using GC equipped with a thermal

conductivity detector. The reaction was conducted for 90 min, and the sulfur capacity was calculated using Eq. (1) [14].

$$\text{Sulfur capacity, mgS/g-sorbent} = (F_{cos} \times M.W_{sulfur}) / W_{sorbent} \times BT \times 1{,}000 \quad (1)$$

Here, F_{COS}, $W_{sorbent}$, and BT are molar flow rate of COS (mol/min), weight of sorbent (g), and breakthrough time (min), respectively. The breakthrough time is defined as the time taken for the COS concentration to reach 5% of the initial value.

4. Computational Details

Theoretical calculations were carried out by DFT calculations using Vienna ab-initio simulation (VASP) [53,54]. The Perdew-Burke-Ernzerhof exchange correlation with the Hubbard U corrections was used with a plane wave expansion cutoff of 600 eV and 400 eV for bulk and surface, respectively [55,56]. The Hubbard parameter U was set to 8.5 [14], and the space group Pn3m was used with monoclinic crystal structure to relax the bulk lattice constants until the forces reached at least 0.01 eV/Å. Four layers were used to model the Cu_2O (111) surface, resulting in approximately 11 Å slab thickness. A 20 Å vacuum layer was placed above the slab to avoid interference between the periodic images of the surface slabs. The bottom two layers were fixed, and the other atoms were allowed to be relaxed until the force reached at least 0.03 eV/Å. The 3×3 unit cell was employed, and 2×2×1 Monkhorst-Pack k-point sample and 8×8×8 Monkhorst-Pack k-point sample were used for the surface and bulk, respectively.

We focused on the Cu_2O (111) surface because it is found to be a stable surface of Cu_2O by both the experimentally and computationally [57,58]. As shown in Fig. 1, four potential active sites were set: top, hcp, fcc, and bridge sites for Cu_2O (111) pristine surface. The top site corresponds to coordinately unsaturated Cu (Cu_{cus}). The effects of the surface sulfur and surface oxygen vacancies on COS absorption reaction toward CO_2 were also examined by introducing an O vacancy and a surface S atom to the Cu_2O (111) surface. Fig. 1 shows the described O vacancy and surface S atom-employed Cu_2O (111) surfaces. The adsorption energy, E_{ads}, of an absorbed molecule (CO, COS, CO_2) on the Cu_2O (111) surface was

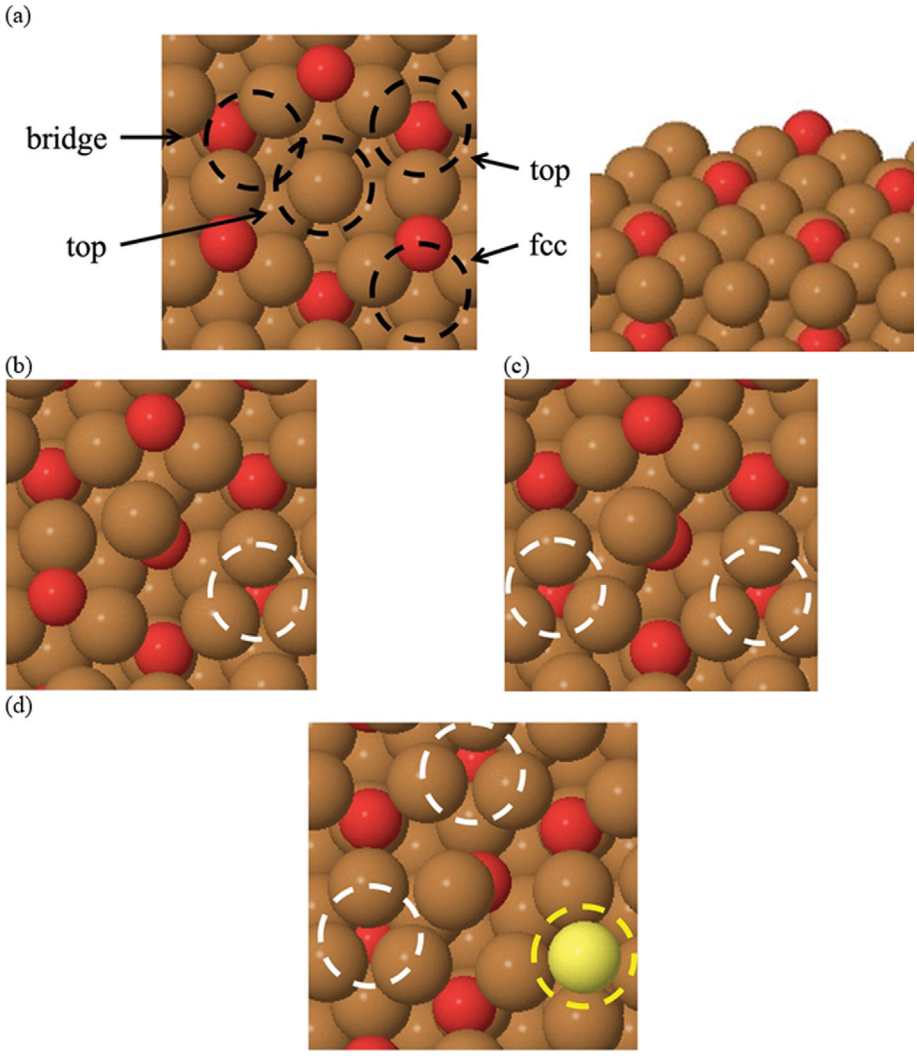

Fig. 1. (a) Top view and side view of Cu_2O (111) pristine surface with the site descriptions. Top view of surface with (b) 1 O vacancy surface (1Ov-surface), (c) 2 O vacancies (2Ov-surface), and (d) both 2 O vacancy and S substitution (2Ov&S-surface). Each O vacancy (white) and surface S atom (yellow) are indicated by the dashed circles.

defined using Eq. (2).

$$E_{ads}=E_{slab}+E_{mol}-E_{mol/slab} \quad (2)$$

The slab energy, E_{slab}, is the energy of the Cu_2O (111) bare surface, and the molecular energy, E_{mol}, is the energy of molecules, CO, COS, and CO_2 as gas phase isolated molecules. $E_{mol/slab}$ is the energy when the molecule is adsorbed on the Cu_2O (111) surface. The large positive value for the adsorption energy indicates high stability of the adsorbed molecule under consideration.

The partial density of states (pDOS) of the d orbitals of Cu atoms was examined to understand the mechanism for CO adsorption on the Cu_2O (111) surface. The projected crystal orbital Hamilton population (pCOHP) method was used to analyze the CO-Cu orbital interaction in the systems. The pCOHP provides a measure of the overlap between the specific atomic orbitals, indicating the bonding, antibonding, and nonbonding contributions. Therefore, they can provide the relative quantification of the bonding [59-61]. LOBSTER software was used to obtain the pCOHP from the VASP output [62].

EXPERIMENTAL RESULTS

1. Copper Aerogels

We investigated X-ray diffraction (XRD) patterns of the aerogels to examine their crystallinity. Fig. 2 shows the XRD patterns of the three differently dried samples (FD, OSSD (ACN), and OSSD (TB)). The FD and OSSD (TB) provide a similar XRD pattern of Cu in which major peaks are present at 43.32°, 50.45°, and 74.13° corresponding to (111), (200), and (220) crystal planes, respectively (JCPDS card no.: 85-1326). In addition, another peak at 36.52° indicates the presence of Cu_2O in both samples (JCPDS card no.: 78-2076), suggesting that the partial oxidation of Cu to Cu_2O occurred during the drying step.

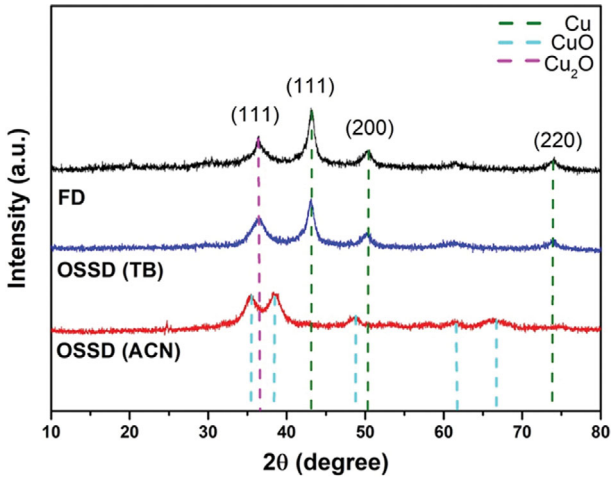

Fig. 2. XRD patterns of three differently dried copper aerogels.

In contrast to the XRD results of FD and OSSD (TB), the XRD peaks of OSSD (ACN) show the CuO phase at 35.54°, 38.85°, 48.96°, 61.73°, and 66.85° corresponding to the (002), (111), ($\bar{2}$02), ($\bar{1}$13), and (220) crystal planes, respectively (JCPDS card no.: 48-1548). The presence of the CuO phase in the ACN sample suggests that the crystalline copper phase is fully oxidized during the drying step. The FD sample was annealed at various temperatures to correlate the oxidation state of copper and the network-like structure of the aerogel (see sec S1 in supporting information SI). The results show

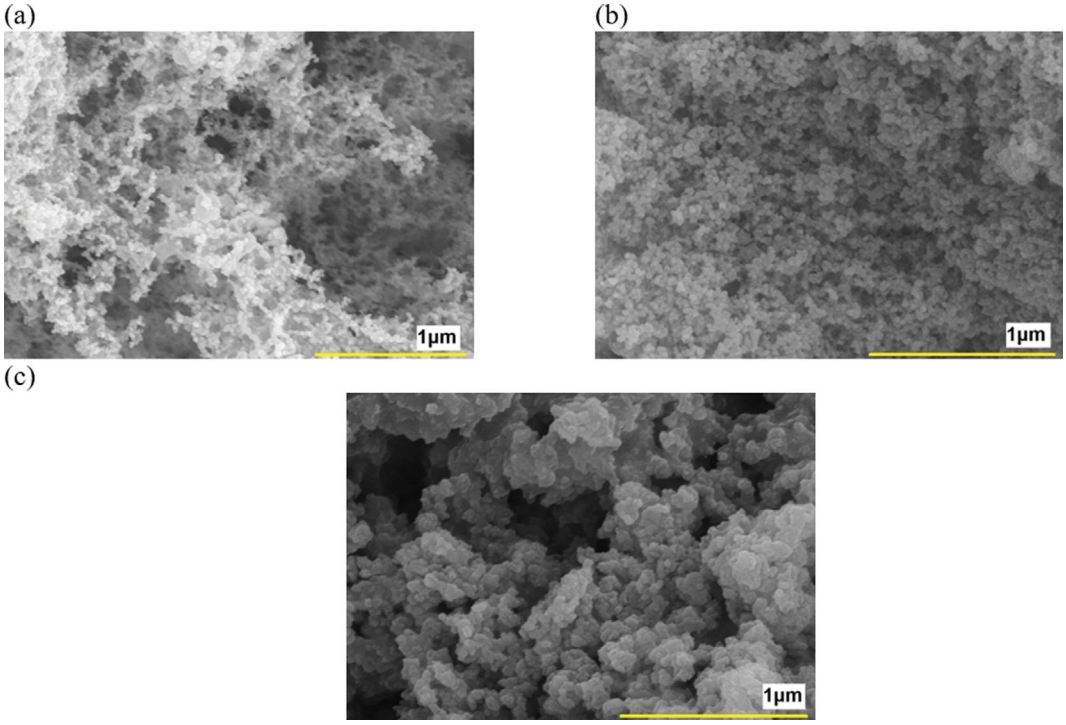

Fig. 3. SEM images of copper aerogel at room temperature, dried by (a) FD (b) OSSD (TB) (c) OSSD (ACN).

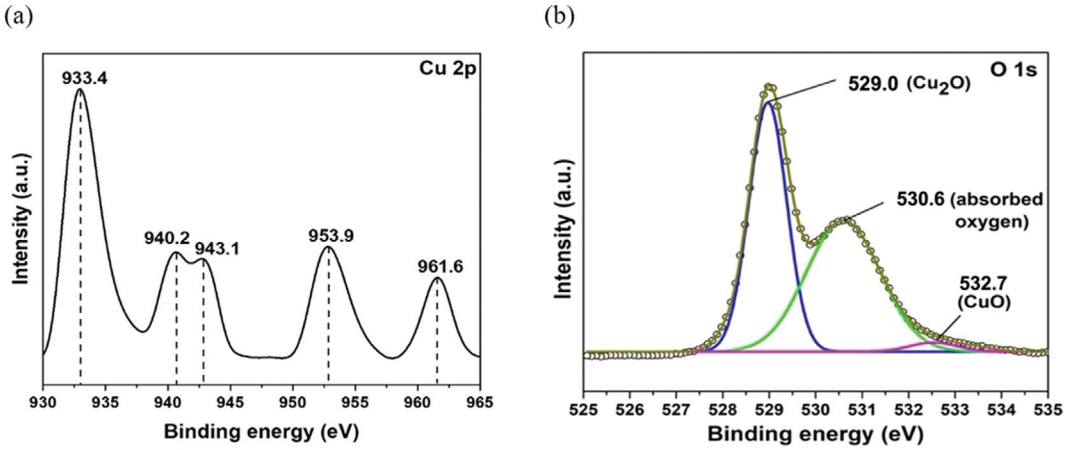

Fig. 4. (a) XPS pattern of copper aerogel (Cu 2p) and (b) oxygen (O 1s) of Cu/Cu_2O. *Freeze-dried copper aerogel.

that the aerogel structure collapses as the copper phase oxidizes. The network-like structure was no longer present in the samples annealed at temperatures higher than 200 °C. These results suggest that the OSSD (ACN) sample lost its network-like structure during the drying step because of the full oxidation of Cu to CuO.

The different oxidation states of the samples may be caused by different drying solvents in the OSSD method. Ren et al. originally introduced the OSSD method as a new drying technique for the formation of inorganic oxide aerogels, and they were applied to the synthesis of SiO_2, Al_2O_3, Fe_2O_3, and NiO aerogels [63]. In addition, extensive studies have been conducted to synthesize the oxide aerogels using the OSSD method, and the oxidation states varied depending on the organic solvents used [63-67].

SEM revealed the structure and morphology of the copper aerogel. Fig. 3 shows the corresponding results for the prepared samples. Fig. 3(a) presents an SEM image of a sample prepared using the FD method showing typical interconnecting structures of an aerogel [68]. The particle sizes range from 5 nm to 10 nm interconnect and form a network-like structure. When the hydrogel sample was rapidly frozen by DI water in a deep freezer (−80 °C) to form the Cu aerogel using the FD method, the high rate of condensation triggered the nonuniform pore size [69]. In addition, the FD hindered the collapse and upheld the hydrogel structure, resulting in distinctive entangled structures of the final aerogel product. Similar structures by the FD method for other metal aerogels have been reported. Bigall et al. prepared Pd aerogels using the FD method and achieved a highly porous, non-ordered, and interconnected structure [70]. Zhang et al. applied the FD method for synthesizing silica aerogels, and also reported network-like structures with mesopores [71]. Fig. 3(b) and (c) show SEM images of the samples treated using the OSSD method with TB and ACN organic solvents, respectively. OSSD (TB) also shows a small particle size between 5 nm and 10 nm with uniformly distributed pores. On the other hand, the particles do not form a network-like structure as the particles prepared using the FD method do. In contrast, OSSD (ACN) does not provide interconnecting structures, and larger particle sizes are observed (>20 nm). The observed large particle size is attributed to the sintering process oxidizing the samples.

XPS was performed to confirm the oxidation states of the sample prepared by FD, showing the presence of Cu_2O. As the survey scan of the Cu 2p core level shows (Fig. 4(a)), the Cu $2p_{3/2}$ and Cu $2p_{1/2}$ peaks are mainly present at binding energies of 933.4 and 953.9 eV, respectively. These peaks are characteristic of Cu_2O moieties and are assigned to Cu(0)/Cu(I) in Cu/Cu_2O aerogel. Three extra shake-up satellite peaks were observed at higher binding energy values, i.e., 940.2, 943.1, and 961.6 eV corresponding to the Cu^{2+} moiety of Cu $2p_{3/2}$ and Cu $2p_{1/2}$, respectively. It implies the presence of an unfilled Cu $3d^9$ shell, which further indicates the presence of a small amount of Cu^{2+} on the sample surface [72]. In the O 1s XPS spectrum (Fig. 4(b)), the peak at a binding energy of 529.0 eV indicates the presence of oxygen in Cu_2O and the peak at 530.6 eV denotes the other absorbed oxygen species in the aerogel. The weak peak at 532.7 eV denotes that the CuO is present in the copper aerogels [73,74].

From characterization studies, including XRD, SEM, and XPS above, the sample prepared by the FD method includes Cu_2O with a network-like structure. These experimental findings imply that the copper aerogels developed by the FD method provide high desulfurization performance. This is because the desulfurization reaction is more favorable with Cu_2O compared to the CuO, and the network-like structure would weaken the diffusion resistance.

The surface area and pore size of each copper aerogel sample were evaluated using nitrogen adsorption-desorption methods in Fig. 5(a), (b), and (c). All isotherms represent type-IV, suggesting that many mesopores are present in copper aerogel [69]. Regardless of the drying methods, copper aerogels have a similar surface area of approximately 40 m^2/g based on BET analysis (Fig. 5(d) and Table 1). In addition, the mean pore diameters of the three differently made copper aerogels are in the range of 16-18 nm (Table 1)

Table 1. BET results of differently dried samples (FD, OSSD (TB), and OSSD (ACN))

Samples	Surface area (m^2/g)	Total pore volume (cm^3/g)	Pore diameter (nm)
FD	39.58	0.19	18.73
OSSD (TB)	41.66	0.18	16.61
OSSD (ACN)	44.38	0.21	18.86

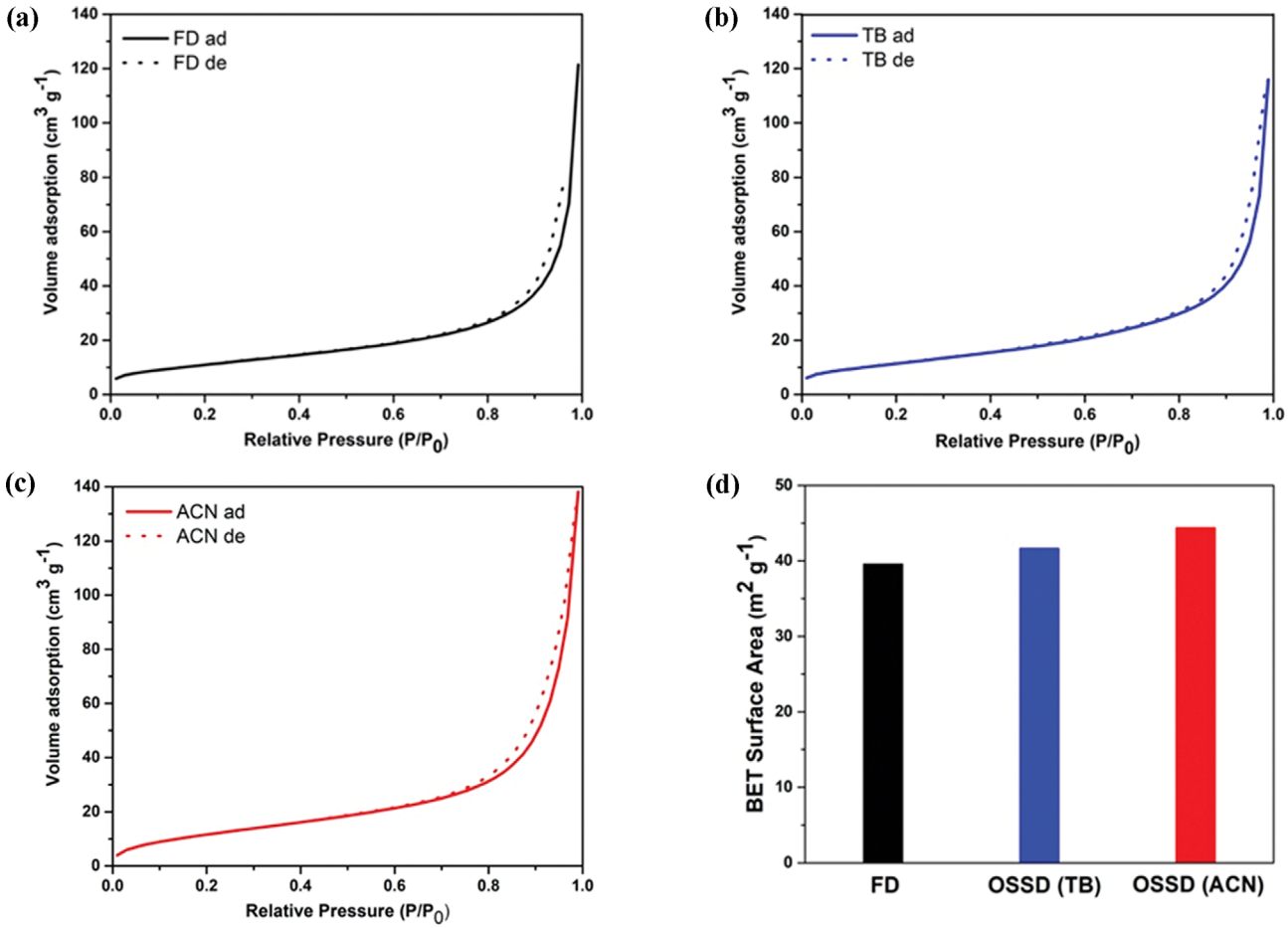

Fig. 5. BET adsorption/desorption graph (a) FD (b) OSSD (TB) (c) OSSD(ACN) (d) BET surface area.

[69]. The FD-treated sample shows the lowest surface area compared to the others, but the gaps in surface area are negligible (<5 m^2/g). Although the FD method did not significantly impact the micro and mesoporous structures, as observed in the SEM image (Fig. 3(a)), a macroporous network-like structure was formed.

2. Desulfurization Tests

We focused on low-temperature desulfurization because thermodynamics drives the similar sulfur capacities of absorbents at high temperatures. The prepared samples (absorbents) were tested at 200 °C and the results are provided in Fig. 6. COS(g) were not monitored by GC at the beginning of the experiment since the COS(g) were well absorbed on Cu aerogels. After reaching a certain time, however, the COS(g) peak increased rapidly (breakthrough (BT) time) due to the limited maximum sulfur capacity of absorbents at 200 °C. The longer (shorter) BT time indicates the higher (lower) sulfur capacity of the absorbents. The effects of aerogel structure will be confirmed by the direct comparison between the experimental results of FD and OSSD (TB). Note that a desulfurization test for OSSD (ACN) was not conducted because the OSSD (ACN) sample showed different oxidation states (CuO) and lost its structure, which is hard to be regarded as copper aerogels. The results show that the FD provides higher desulfurization performance (30 minutes BT time and a sulfur capacity of 12 mgS/g-sorbent) compared to the OSSD (TB). The higher performance of FD stems from the distinctive network-like structure (Fig. 3), which facilitates gas diffusion. Hence, the COS gas flows deep inside the FD

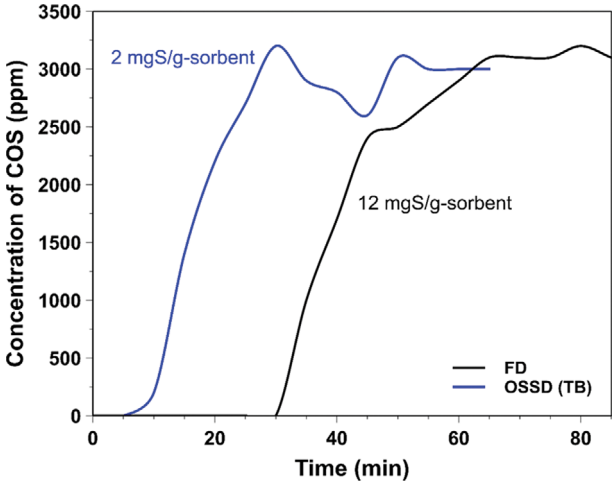

Fig. 6. COS breakthrough curves of the desulfurization test result by gas chromatography, including the results of FD sample (black line) and OSSD (TB) sample (blue line). The indicated values are the calculated sulfur capacities using the breakthrough time and the Eq. (1) above.

sample, resulting in an improved sulfur capacity of the absorbent.

In contrast to the FD sample, the OSSD (TB) sample provided a short breakthrough time of 5 min. The origin of the poor performance of OSSD (TB) was the absence of a network-like structure. As shown in Fig. 2, the OSSD (TB) and FD both have Cu_2O, but only the FD sample has a network-like structure. Recent work on the desulfurization absorbent also provided similar results [14]. The presence of macropores significantly enhances the sulfur capacity of an absorbent with lower surface areas and pore sizes than the other absorbents without macropores. Therefore, the direct comparison results suggest that the better performance of FD stems from the network-like structure due to the decrease in the gas diffusion resistance.

The presence of Cu_2O would influence both samples because Cu_2O is thermodynamically preferred to CuO for desulfurization reactions. We fundamentally investigated the desulfurization kinetics on the Cu_2O absorbent by DFT simulations to elucidate the role of the Cu_2O phase in the FD and OSSD (TB) sample. Therefore, it is expected that a network-like structure (decrease in the diffusion resistance) and Cu_2O (more active toward desulfurization than CuO) cooperatively improves the desulfurization performance of copper absorbent.

3. Computational Result and Analysis

3-1. Stability of Desulfurization Intermediates

The three different surfaces of Cu_2O (111) with one oxygen vacancy (1Ov-surface) and two oxygen vacancies (2Ov-surface) and the surface with two oxygen vacancies and a sulfur atom (2Ov&S-surface) were explored to consider the effects of the local environment. Surface oxygen vacancies must be present because COS dissociation requires the oxygen vacancy (COS*+Ov→

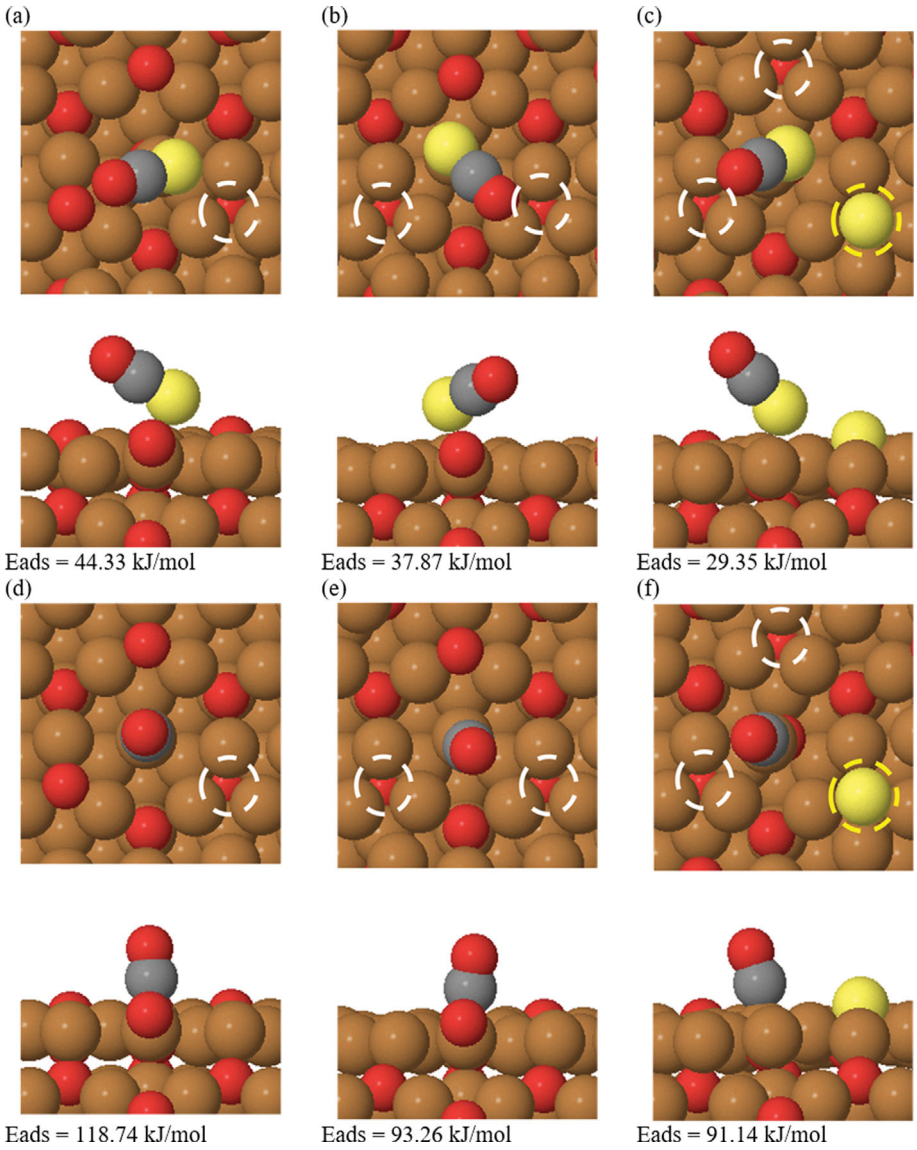

Fig. 7. Top and side views of absorbed COS, and CO on each Cu_2O (111) 1Ov-surface, 2Ov-surface, and 2Ov&S-surface. The white dashed line indicates oxygen vacancy, and the yellow dashed line indicates a sulfur-substituted atom. The DFT predicted adsorption energy is presented below each figure.

CO*+S*), and the presence of Ov and the generated surface sulfur would affect the desulfurization kinetics. The stability of adsorbed desulfurization intermediates molecules (COS and CO) on the three surfaces was evaluated by calculating the adsorption energy. The Cu_2O (111) surface has four potential active sites of top, hcp, fcc, and bridge, as shown in Fig. 1, and the simulation predicted that the molecules on the top sites provide the most favored configuration. The molecules on other sites gradually migrated to the top site during the DFT relaxations, meaning that the configurations of molecules on other sites are unstable. Similar computational predictions were reported in that the linear molecules on the Cu_{cus} (Cu top) site on Cu_2O (111) are most stable [75-77]. Fig. 7 shows the favored configuration of each adsorbed molecule with the corresponding adsorption energy. The adsorbed COS was predicted to weakly bind to the 1Ov-surface with an adsorption energy of 44.33 kJ/mol, and its configuration is tilted toward surface oxygen. The vertical configuration of COS was also tested, and its adsorption energy was predicted to be much lower than the tilted configuration (44.33 kJ/mol vs. 2.04 kJ/mol). This suggests that the tilted configuration experiences stronger interactions with the surface oxygen, thereby forming stronger bonds. When introducing another Ov (2Ov-surface) and surface sulfur atom (2Ov&S-surface), the adsorbed COS becomes slightly destabilized by ~7 kJ/mol and 5 kJ/mol, respectively (see Figs. 7(b) and 7(c)). The comparison results imply that the presence of Ov and surface sulfur both slightly and similarly destabilizes the adsorbed COS in which the destabilization stems from the termination of interaction between surface oxygen and adsorbed COS. In contrast to COS adsorption, CO adsorbs strongly on the 1Ov-surface with high adsorption energy of 118.74 kJ/mol. The CO molecule on the 2Ov-surface and 2Ov&S-surface also indicates high adsorption energy of 93.26 kJ/mol and 91.14 kJ/mol, respectively, with a destabilization of ~20 kJ/mol. The predicted strong binding of CO is chemisorption driven mainly by combinations of a covalent bond (hybridization of molecular orbitals) and ionic bond (electron transfer), which is strongly affected by electronic structures, while COS binding is physisorption-based adsorption, resulting in weak binding. CO destabilization with electronic structure analysis is discussed in the next section.

3-2. Electronic Structural Analysis

Since the presence of Ov destabilizes the adsorbed CO compared to the destabilization by surface sulfur shown in Fig. 7, electronic structure analysis was conducted to understand the origin of CO destabilization by the presence of Ov. The d orbitals were evaluated, including d_{xy+yz}, $d_{x^2-y^2}$, and d_{z^2} of the surface Cu_{cus} atom directly interacting with the adsorbed CO atom. The simulation predicted that the d orbitals were not affected by the presence of Ov; pDOS of 1Ov- and 2Ov-surfaces are similar to each other, as shown in Fig. S3 in SI. These similar pDOS results suggest that the adsorbed CO and Cu_{cus} atom may experience similar donation and back donation interactions on both surfaces; however, the molecular orbitals (bonding and antibonding) between CO and Cu_{cus} might be formed differently to provide the different stability of adsorbed CO. To quantify bonding and antibonding contributions to the CO bindings, pCOHP analysis on the relationship between adsorbed CO and d orbitals of Cu_{cus} atom was additionally performed. Table 2 lists the IpCOHP quantifying bonding and antibonding contributions to the interactions between the adsorbed CO and the Cu_{cus} of 1Ov- and 2Ov surfaces by integrating the COHP values along with the energy levels. A more negative (positive) IpCOHP value indicates stronger (weaker) binding and weaker (stronger) antibonding contribution results in strong (weak) total bonding interactions. The results show that CO on both surfaces undergo the similar antibonding interactions (0.92 vs. 0.93). However, the bonding interactions of CO on 1Ov-surface are slightly stronger than the CO on 2Ov-surface (−3.64 vs. −3.51), resulting in the stronger total interactions (bonding+antibonding). Based on the IpCOHP results, we conclude that the presence of Ov weakens the bonding interactions between CO and Cu_{cus} thereby destabilizing adsorbed CO.

Table 2. Integrated partial crystal orbital Hamiltonian populations (IpCOHP) results of CO molecules on Cu_{cus} for 1Ov-surface and 2Ov-surfaces. The more negative (positive) value means stronger (antibonding) bonding interaction

	Total	Bonding	Antibonding
1Ov-surface	−2.72	−3.64	0.92
2Ov-surface	−2.59	−3.51	0.93

3-2. Desulfurization Kinetics

The mechanism of desulfurization reaction steps is followed as below three steps [14]. 1) COS gas molecule adsorbs on Cu_2O (111) surface, 2) COS^* is decomposed into CO^* and S^* on the surface (* indicates the adsorption.). 3) CO^* then reacts to an adjacent surface oxygen and produce CO_2^* with CO_2 (g) desorption.

$$COS\ (g)+* \rightarrow COS^* \text{ (step 1)}$$
$$COS^*+1Ov \rightarrow CO^*+S^* \text{ (step2)}$$
$$CO^*+S^*+O_{surf} \rightarrow CO_2^*+S^* \text{ (step3)}$$

We evaluated the Gibbs free energies of the initial and final states of each elementary step in the above mechanism on the three different surfaces of 1Ov-surface, 2Ov-surface, and 2Ov&S-surface. Note that the proposed Gibbs free energy diagrams do not include the energy barriers, and we focused on the thermodynamic preferences of the COS desulfurization kinetics on Cu_2O (111) surface. Fig. 8 provides the computed Gibbs free energy for COS desulfurization reactions on the three different surfaces. The results show that on the 1Ov-surface, the adsorption of COS(g) on the Cu_2O (111) surface was predicted to be thermodynamically unfavorable. On the other hand, subsequent reactions show a significant thermodynamic preference (ΔG: −104.49 kJ/mol). Similar thermodynamic behavior had been predicted on the other two surfaces, but the ΔG of COS^* decomposition ($COS^* \rightarrow CO^*+S^*$) decreased dramatically on the 2Ov-surface and 2Ov&S-surface because of the considerable stabilization for the CO^*+S^*. The significant decreases in ΔG make the COS bond cleavage facile, accelerating the overall desulfurization kinetics. Thus, the desulfurization rate would accelerate as the desulfurization reaction proceeds, which increase the concentration of surface S and Ov. Similar thermodynamic behavior was found on the CuO (111) surface, which stems from the stabilized CO^* by adjacent surface S and Ov [14]. Based on similar predicted behavior, the behavior might be universal for COS

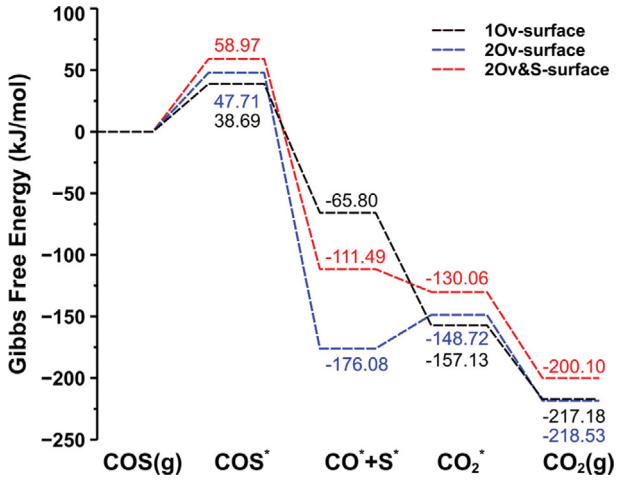

Fig. 8. Gibbs Free energy diagram of desulfurization reaction on Cu_2O (111) surface. Black, blue, and red dashed lines are the reactions on 1Ov-surface, 2Ov-surface, and 2Ov&S-surface, respectively.

desulfurization on copper-based absorbents (CuO, Cu_2O). Future studies will examine the COS desulfurization kinetics on other facets of copper-based absorbents to confirm the effects of surface S and Ov.

The overall desulfurization reactions are thermodynamically favorable ($\Delta G \approx -210$ kJ/mol) regardless of the local environment on Cu_2O. A comparison of the results of COS desulfurization on the CuO surface shows that the thermodynamics favors desulfurization on Cu_2O over CuO [14]. It further suggests that the highly favorable thermodynamics drives the high activity toward the desulfurization kinetics on Cu_2O compared to CuO. These results support the experimental desulfurization results for a steep rise of the breakthrough curve. In addition, the results correspond to the results from other research applying Cu_2O for adsorptive desulfurization with various methods, such as structural modification of Cu_2O or manufacturing by mixing other materials [27,28,78,79]. They also show excellent performance in desulfurization reactions, and are well consistent with our experimental and computational results. Overall, the experimental and computational results confirm that the higher performance of FD stems from the Cu_2O phase (favorable thermodynamics) and network-like structure (weakened diffusion resistance).

CONCLUSION

Copper aerogels were synthesized using three different drying methods: freeze drying and organic solvent sublimation drying with tert-butanol and acetonitrile to develop high performance of desulfurization absorbents. The freeze-dried copper aerogels have the typical aerogel feature of a network-like structure and show the highest performance desulfurization (30 minutes breakthrough time with the 12 mgS/g-sorbent of sulfur capacity). The high performance of FD stems from the presence of distinctive interconnecting structure as aerogel enabling to weaken gas diffusion resistance (GDR), and the presence of Cu_2O allowing COS desulfurization reaction to be thermodynamically facile.

Overall, this novel approach using the network-like structure of aerogels and the active phase of Cu_2O provides significant improvement in the desulfurization reaction. Based on these results, we conclude that copper aerogel would be a good candidate for a desulfurization absorbent. Further efforts should be made to achieve higher performance, reusability, and stability. For instance, it would be non-trivial to regenerate Cu aerogel absorbent to be reused because the regeneration process typically requiring high temperature leads to full oxidation of Cu aerogel, resulting in the decomposition of network-like temperature. In addition, using support with aerogel, for instance, would dramatically increase surface area, which leads to higher sulfur capacity. The experimentally and computationally verified potential of a copper aerogel for desulfurization highlights the need for further optimization.

ACKNOWLEDGEMENTS

This work was supported by Priority Research Centers Program funded by the Ministry of Education (2014R1A6A1031189), a grant (22PCHG-C161574-02) from Development of Demonstration-scale Hydrogen Production Technology using Petroleum coke Program funded by Ministry of Land, Infrastructure and Transport of Korea government, and 2021 Yeungnam University Research Grant. This work was also supported by the Basic Science Research Program (2020R1I1A3051997) through the National Research Foundation of Korea (NRF) funded by the Ministry of Education.

SUPPORTING INFORMATION

Additional information as noted in the text. This information is available via the Internet at http://www.springer.com/chemistry/journal/11814.

REFERENCES

1. P. Nikolaidis and A. Poullikkas, *Renew. Sustain. Energy Rev.*, **67**, 597 (2017).
2. P. P. Edwards, V. L. Kuznetsov and W. I. F. David, *Philos. Trans. R. Soc. A Math. Phys. Eng. Sci.*, **365**, 1043 (2007).
3. M. Noussan, P. P. Raimondi, R. Scita and M. Hafner, *Sustainability*, **13**, 298 (2021).
4. I. Dincer, *Int. J. Hydrogen Energy*, **37**, 1954 (2012).
5. S. Atilhan, S. Park, M. M. El-Halwagi, M. Atilhan, M. Moore and R. B. Nielsen, *Curr. Opin. Chem. Eng.*, **31**, 100668 (2021).
6. Z. Navas-Anguita, D. García-Gusano, J. Dufour and D. Iribarren, *Sci. Total Environ.*, **771**, 145432 (2021).
7. M. H. Ali Khan, R. Daiyan, P. Neal, N. Haque, I. MacGill and R. Amal, *Int. J. Hydrogen Energy*, **46**, 22685 (2021).
8. M. Yu, K. Wang and H. Vredenburg, *Int. J. Hydrogen Energy*, **46**, 21261 (2021).
9. R. W. Howarth and M. Z. Jacobson, *Energy Sci. Eng.*, **9**, 1676 (2021).
10. B. N. Murthy, A. N. Sawarkar, N. A. Deshmukh, T. Mathew and J. B. Joshi, *Can. J. Chem. Eng.*, **92**, 441 (2014).
11. V. Nemanova, A. Abedini, T. Liliedahl and K. Engvall, *Fuel*, **117**, 870 (2014).

12. J. Wei, Q. Guo, Y. Gong, L. Ding and G. Yu, *Renew. Energy*, **155**, 111 (2020).
13. N. Nipattummakul, I. I. Ahmed, S. Kerdsuwan and A. K. Gupta, *Int. J. Hydrogen Energy*, **35**, 11738 (2010).
14. D. Kim, D. Bae, Y. J. Kim, S. J. Lee, J. W. Lee, Y. Yun, N.K. Park and M. Kim, *Appl. Sci.*, **11**, 7775 (2021).
15. I. V. Babich and J. A. Moulijn, *Fuel*, **82**, 607 (2003).
16. B. Saha, S. Vedachalam and A. K. Dalai, *Fuel Process. Technol.*, **214**, 106685 (2021).
17. H. Kuwahara, *Chem. Econ. Engng Rev.*, **5**, 35 (1973).
18. H. Bin Fang, J. T. Zhao, Y. T. Fang, J. J. Huang and Y. Wang, *Fuel*, **108**, 143 (2013).
19. D. Jiang, L. Su, L. Ma, N. Yao, X. Xu, H. Tang and X. Li, *Appl. Surf. Sci.*, **256**, 3216 (2010).
20. K. M. Dooley, V. Kalakota and S. Adusumilli, *Energy Fuels*, **25**, 1213 (2011).
21. R. Menzel, D. Iruretagoyena, Y. Wang, S. M. Bawaked, M. Mokhtar, S. A. Al-Thabaiti, S. N. Basahel and M. S. P. Shaffer, *Fuel*, **181**, 531 (2016).
22. J. Wang, L. Wang, H. Fan, H. Wang, Y. Hu and Z. Wang, *Fuel*, **209**, 329 (2017).
23. J. Abbasian and R. B. Slimane, *Ind. Eng. Chem. Res.*, **37**, 2775 (1998).
24. M. H. Morcali, B. Zeytuncu, A. Baysal, S. Akman and O. Yucel, *J. Environ. Chem. Eng.*, **2**, 1655 (2014).
25. Y. Wang, F. H. Yang and R. T. Yang, *Ind. Eng. Chem. Res.*, **45**, 7649 (2006).
26. W. H. Tian, L. B. Sun, X. L. Song, X. Q. Liu, Y. Yin and G. S. He, *Langmuir*, **26**, 17398 (2010).
27. S. Liu, B. Zhang, Z. Bai, F. Chen, F. Xie, J. Zhou, Y. Lu, G. Miao, J. Jin and Z. Zhang, *Energy Fuels*, **32**, 13004 (2018).
28. T. Feng, Y. Wang, Y. N. Wu, D. M. Kabtamu, K. László and F. Li, *J. Mater. Chem. A.*, **8**, 8678 (2020).
29. I. Nitta, O. Himanen and M. Mikkola, *Electrochem. Commun.*, **10**, 47 (2008).
30. J. Shen, J. Zhou, N. G. C. Astrath, T. Navessin, Z. S. Liu, C. Lei, J. H. Rohling, D. Bessarabov, S. Knights and S. Ye, *J. Power Sources*, **196**, 674 (2011).
31. T. Mashio, A. Ohma, S. Yamamoto and K. Shinohara, *ECS Trans.*, **11**, 529 (2007).
32. J. Jiao, J. Cao, Y. Xia and L. Zhao, *Chem. Eng. J.*, **306**, 9 (2016).
33. Z. Zhao, X. Cui, J. Ma and R. Li, *Int. J. Greenh. Gas Control.*, **1**, 355 (2007).
34. N. Jia, R. B. Martin, Z. Qi, M. C. Lefebvre and P. G. Pickup, *Electrochemica Acta*, **46**, 2863 (2001).
35. O. Celikbilek, C. A. Thieu, F. Agnese, E. Calì, C. Lenser, N. H. Menzler, J. W. Son, S. J. Skinner and E. Djurado, *J. Mater. Chem. A.*, **7**, 25102 (2019).
36. N. Fang, J. Guo, S. Shu, H. Luo, Y. Chu and J. Li, *Chem. Eng. J.*, **325**, 114 (2017).
37. R. Rao, Q. Zhang, H. Liu, H. Yang, Q. Ling, M. Yang, A. Zhang and W. Chen, *J. Mol. Catal. A Chem.*, **363-364**, 283 (2012).
38. M. N. Hossain, Z. Liu, J. Wen and A. Chen, *Appl. Catal. B Environ.*, **236**, 483 (2018).
39. Y. Jing, L. Wei, Y. Wang and Y. Yu, *Micropor. Mesopor. Mater.*, **183**, 124 (2014).
40. G. B. Baur, I. Yuranov and L. Kiwi-Minsker, *Catal. Today*, **249**, 252 (2015).
41. K. Ganesan, T. Budtova, L. Ratke, P. Gurikov, V. Baudron, I. Preibisch, P. Niemeyer, I. Smirnova and B. Milow, *Materials (Basel)*, **11**, 1 (2018).
42. I. Smirnova and P. Gurikov, *J. Supercrit. Fluids*, **134**, 228 (2018).
43. A. Du, B. Zhou, Z. Zhang and J. Shen, *Materials (Basel)*, **6**, 941 (2013).
44. A. Soleimani Dorcheh and M. H. Abbasi, *J. Mater. Process. Technol.*, **199**, 10 (2008).
45. S. N. Schiffres, K. H. Kim, L. Hu, A. J. H. McGaughey, M. F. Islam and J. A. Malen, *Adv. Funct. Mater.*, **22**, 5251 (2012).
46. M. Glora, M. Wiener, R. Petričević, H. Pröbstle and J. Fricke, *J. Non-Cryst. Solids*, **285**, 283 (2001).
47. J. Biener, M. Stadermann, M. Suss, M. A. Worsley, M. M. Biener, K. A. Rose and T. F. Baumann, *Energy Environ. Sci.*, **4**, 656 (2011).
48. L. Ren, S. Cui, F. Cao and Q. Guo, *Angew. Chem. - Int. Ed.*, **53**, 10147 (2014).
49. L. Hu, R. He, Z. Lu, K. Zhang and X. Bai, *RSC Adv.*, **9**, 9931 (2019).
50. M. Georgi, B. Klemmed, A. Benad and A. Eychmüller, *Mater. Chem. Front.*, **3**, 1586 (2019).
51. E. J. Beckman, *J. Supercrit. Fluids*, **28**, 121 (2004).
52. S. Alwin and X. Sahaya Shajan, *Mater. Renew. Sustain. Energy*, **9**, 1 (2020).
53. R. A. Vargas-Hernández, *J. Phys. Chem. A.*, **124**, 4053 (2020).
54. G. Kresse and J. Furthmüller, *Comput. Mater. Sci.*, **6**, 15 (1996).
55. S. Dudarev and G. Botton, *Phys. Rev. B - Condens. Matter Mater. Phys.*, **57**, 1505 (1998).
56. J. P. Perdew, K. Burke and M. Ernzerhof, *Phys. Rev. Lett.*, **77**, 3865 (1996).
57. A. Soon, M. Todorova, B. Delley and C. Stampfl, *Phys. Rev. B - Condens. Matter Mater. Phys.*, **75**, 1 (2007).
58. X. Yu, X. Zhang, H. Wang, Z. Wang and G. Feng, *J. Phys. Chem. C.*, **121**, 22081 (2017).
59. V. L. Deringer, A. L. Tchougréeff and R. Dronskowski, *J. Phys. Chem. A.*, **115**, 5461 (2011).
60. R. Dronskowski, M. Festkbrperforschung and P. E. Blochl, *J. Phys. Chem.*, **97**, 8617 (1993).
61. S. Maintz, V. L. Deringer, A. L. Tchougréeff and R. Dronskowski, *J. Comput. Chem.*, **34**, 2557 (2013).
62. S. Maintz, V. L. Deringer, A. L. Tchougréeff and R. Dronskowski, *J. Comput. Chem.*, **37**, 1030 (2016).
63. X. Li, H. He, S. Cui and L. Ren, *ECS J. Solid State Sci. Technol.*, **5**, N1 (2016).
64. L. Ren, X. Li and S. Cui, *J. Nanomater.*, **2016**, 1 (2016).
65. X. guang Liu, Q. shuo Mao, Y. Jiang, Y. Li, J. lin Sun and F. xue Huang, *Int. J. Miner. Metall. Mater.*, **28**, 317 (2021).
66. J. Gao, W. Wei, M. J. Shi, H. Han, J. Lu and J. Xie, *J. Mater. Sci.*, **51**, 4481 (2016).
67. Y. Wu, H. Jiang, F. S. Ke and H. Deng, *Chem. - An Asian J.*, **14**, 3577 (2019).
68. Y. Bi, H. Ren, B. Chen, G. Chen, Y. Mei and L. Zhang, *J. Sol-Gel Sci. Technol.*, **63**, 140 (2012).
69. S. He, D. Huang, H. Bi, Z. Li, H. Yang and X. Cheng, *J. Non-Cryst. Solids*, **410**, 58 (2015).
70. A. Freytag, S. Sánchez-Paradinas, S. Naskar, N. Wendt, M. Colombo, G. Pugliese, J. Poppe, C. Demirci, I. Kretschmer, D. W. Bahnemann,

P. Behrens and N. C. Bigall, *Angew. Chem. - Int. Ed.*, **55**, 1200 (2016).
71. Y. Pan, S. He, L. Gong, X. Cheng, C. Li, Z. Li, Z. Liu and H. Zhang, *Mater. Des.*, **113**, 246 (2017).
72. M. Yin, C. K. Wu, Y. Lou, C. Burda, J. T. Koberstein, Y. Zhu and S. O'Brien, *J. Am. Chem. Soc.*, **127**, 9506 (2005).
73. Y. Gao, F. Yang, Q. Yu, R. Fan, M. Yang, S. Rao, Q. Lan, Z. Yang and Z. Yang, *Microchim. Acta*, **186**, 192 (2019).
74. Y. C. Huang, C. H. Chou, C. Y. Liao, W. L. Tsai and H. C. Cheng, *Appl. Phys. Lett.*, **103**, 1 (2013).
75. F. Chiter, D. Costa, V. Maurice and P. Marcus, *J. Phys. Chem. C*, **124**, 17048 (2020).
76. T. Le, Y. Shao and B. Wang, *J. Phys. Chem. C.*, **125**, 6108 (2021).
77. L. I. Bendavid and E. A. Carter, *J. Phys. Chem. C.*, **117**, 26048 (2013).
78. Q. Le, Y. Xiang, Z. Liu and Z. Cheng, *Colloids Surf. A Physicochem. Eng. Asp.*, **648**, 129369 (2022).
79. J. Kou, C. Lu, W. Sun, L. Zhang and Z. Xu, *ACS Sustain. Chem. Eng.*, **3**, 3053 (2015).

Supporting Information

Enhanced desulfurization performance of copper aerogel-based absorbents

Jungwon Yun[*,], Dohyung Kang[***], Ramya Ramkumar[*], Dongjoon Kim[**], Seung Jong Lee[****], Yongseung Yun[****], Woo Kyoung Kim[*,†], No-Kuk Park[*****,†], and Minkyu Kim[*,†]**

*School of Chemical Engineering, Yeungnam University, 280 Daehak-ro, Gyeongsan, Gyeongbuk 38541, Korea
**William G. Lowrie Chemical and Biomolecular Engineering, The Ohio State University, Columbus, Ohio 43210, USA
***Department of Future Energy Convergence, Seoul National University of Science & Technology, 232 Gongreung-ro, Nowon-gu, Seoul 01811, Korea
****Institute for Advanced Engineering, 175-28, Goan-ro 51 beon-gil, Baegam-myeon, Cheoin-gu, Yongin-si, Gyeonggi-do 17180, Korea
*****Institute of Clean Technology, Yeungnam University, 280 Daehak-ro, Gyeongsan, Gyeongbuk 38541, Korea
(*Received 27 July 2022 • Revised 19 September 2022 • Accepted 12 October 2022*)

S1. Annealing Experiment of FD Sample

Annealing experiments of as-synthesized copper aerogel (FD) were conducted to produce completely oxidized products, i.e., copper oxide (CuO) materials. The as-synthesized copper aerogel was annealed at 200 °C, 300 °C, 400 °C, and 500 °C to synthesize complete copper oxide. Annealing was processed in a high-temperature furnace with the existence of air. As was intended, complete oxidation of the copper aerogels occurred, resulting in crystalline and nanoparticle-like structures of Cu aerogels.

Fig. S1 denotes annealed copper aerogel, which was dried using the FD method; a higher temperature resulted in a more oxidized sample. Only the copper aerogel annealed at 200 °C demonstrated both patterns of CuO and Cu_2O. The CuO peak is at 35.45°, 38.75°, 38.91°, 48.71°, 53.55°, 58.3°, 61.55°, 65.87°, 66.21°, 66.47°, 68.15°, 68.93°, 72.39°, 75.02°, and 75.28° corresponding to the (002), (111), (200), (202), (020), (202), (113), (022), (311), (310), (220), (221), (311), (004), and (222) crystal planes (JCPDS card no.: 48-1548) of CuO, respectively. The Cu_2O peaks at 36.5°, 42.3°, 61.4°, and 73.6° were assigned to the (111), (220), (220), and (311) crystal planes (JCPDS card no.: 78-2076), respectively. By contrast, the copper aerogel annealed at higher temperatures than 200 °C showed the patterns of mainly CuO. The peak intensities increased at high temperatures, which is consistent with high crystallinities and low surface area.

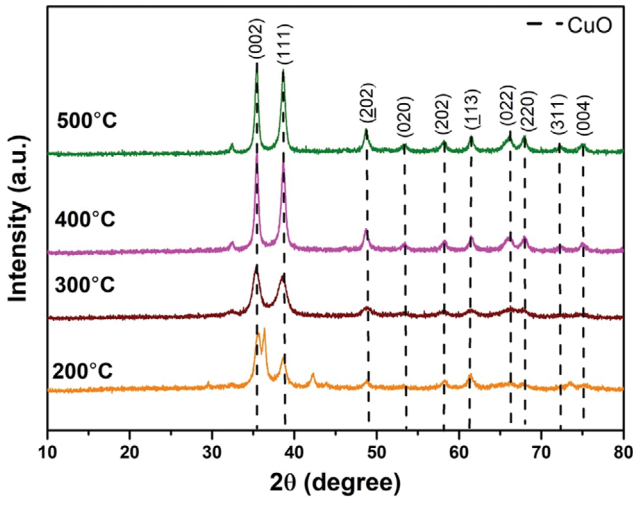

Fig. S1. XRD pattern of the annealed FD sample. The samples were annealed at various temperatures. The black dashed line is CuO JCPDS (no. 48-1548).

Fig. S2 shows SEM images of the annealed FD samples. The metal particles aggregated rather than the non-annealed FD sample. The reactivity between the air and copper aerogel particles increased with increasing temperature, and the sample was more oxidized at high temperatures and sintered due to the characteristics of metals. The network-like structure decomposed after annealing. In addition, the particle sizes became larger, approximately 10 nm. This leads to complete loss of the aerogel structure without high porosity and high surface area and affects the behavior of the nanoparticles.

S2. Density of States for Cu_{cus} Atom

To obtain fundamental insights into the stabilization of adsorbed CO on three different surfaces with regard to the local environments, the electronic structure analysis was performed by exploring the partial density of states (pDOS) of Cu_{cus}. The pDOS of Cu_{cus} for 1Ov-surface, 2Ov-surface, and 2Ov&S-surface are shown in Fig. S3 below. The d orbitals, including d_{xy+yz}, $d_{x^2-y^2}$, and d_{z^2} were evaluated, but the various d bands from the different surfaces provide similar trends. Despite some differences, it was too negligible to explain the trend of stabilization.

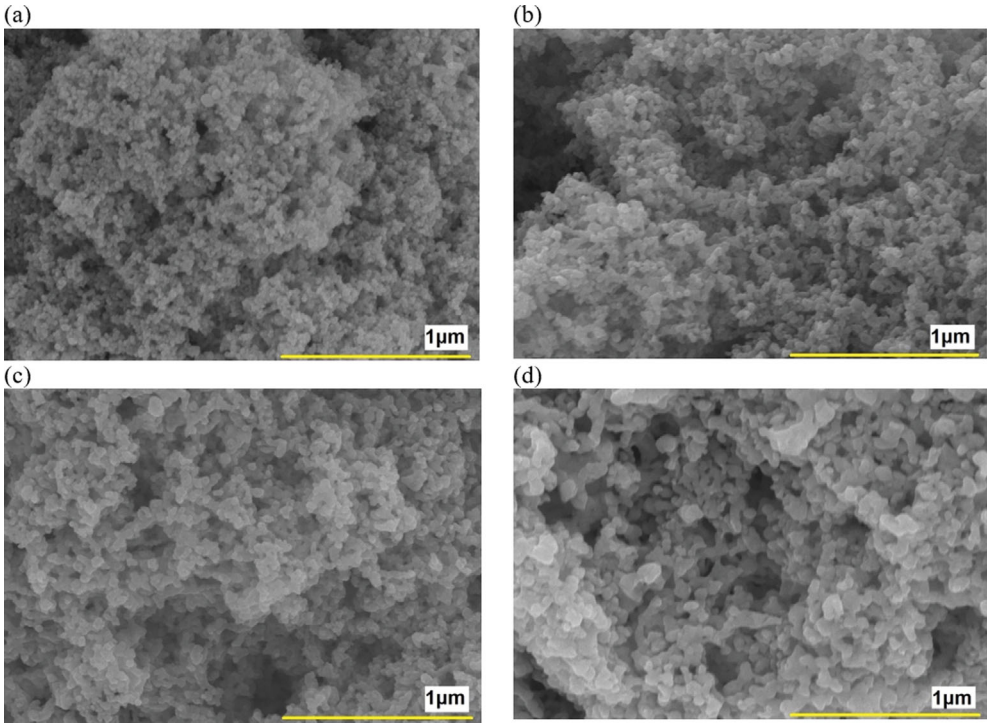

Fig. S2. SEM of annealed FD sample. The sample is annealed at (a) 200 °C, (b) 300 °C, (c) 400 °C, and (d) 500 °C.

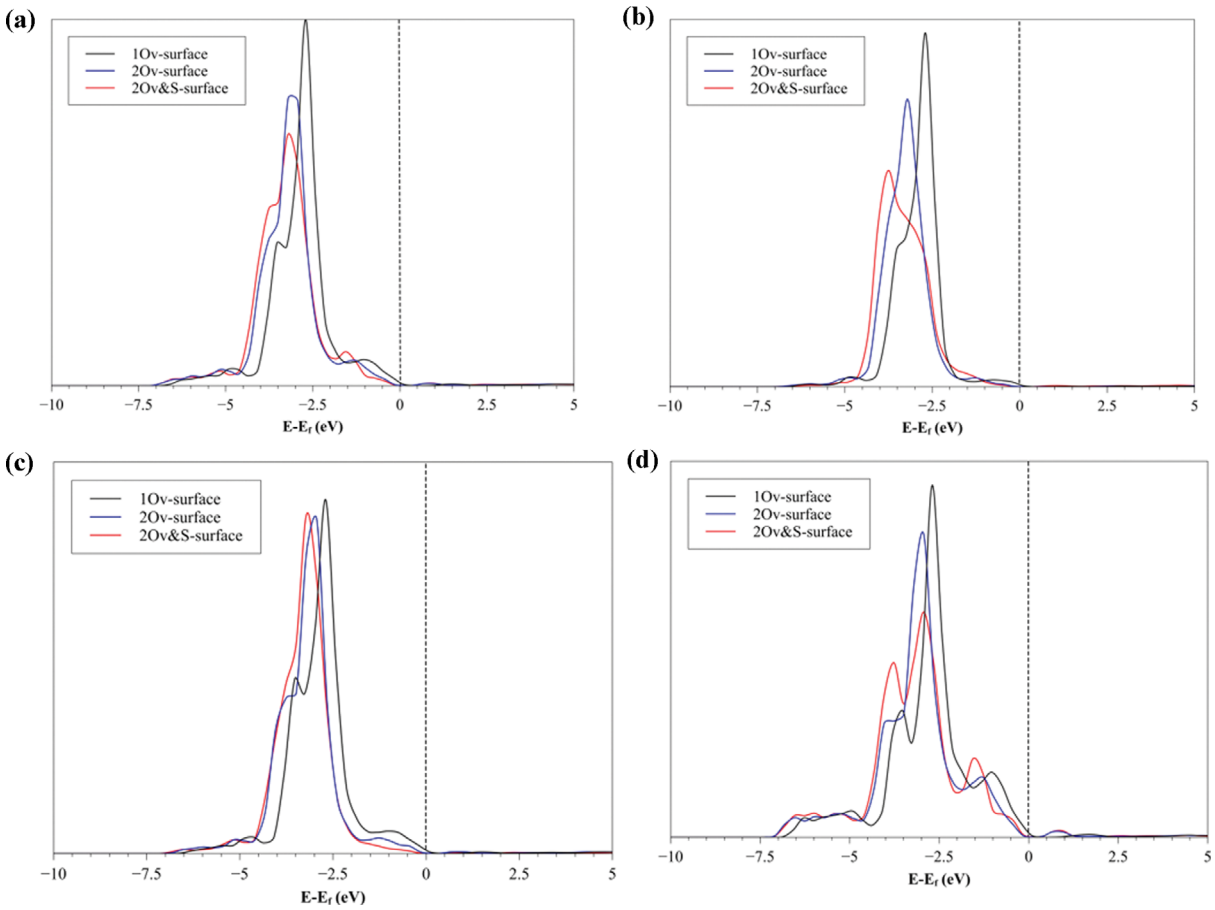

Fig. S3. Projected density of states (pDOS) of (a) d total (sum of d orbitals) (b) d_{xy+yz} (c) $d_{x^2-y^2}$, and (d) d_{z^2} orbitals for a copper atom on top, with respect to the Fermi level. The Fermi level is located at 0 eV and is indicated by the dashed line.